Journal of Magnetic Resonance 391 (2026) 108128

Contents lists available at ScienceDirect

Journal of Magnetic Resonance

journal homepage: www.elsevier.com/locate/jmr

NMR Relaxometry across ultra-wide range fields using atomic magnetometers

Qianyue Qu [a,1], Lianglin Tang [a,b,1], Zeming Li [a,b], Haogang Qi [a], Li Wang [a,b], Liang Xu [b,c], Qi Li [b,c], Yunhuang Yang [a,b], Yinan Hu [a,b], Xin Zhou [a,b,d,*]

[a] State Key Laboratory of Magnetic Resonance Spectroscopy and Imaging, National Center for Magnetic Resonance in Wuhan, Wuhan Institute of Physics and Mathematics, Innovation Academy for Precision Measurement Science and Technology, Chinese Academy of Sciences – Wuhan National Laboratory for Optoelectronics, Huazhong University of Science and Technology, Wuhan 430071, Hubei, China
[b] University of Chinese Academy of Sciences, Beijing 100049, China
[c] State Key Laboratory of Geomechanics and Geotechnical Engineering Safety, Institute of Rock and Soil Mechanics, Chinese Academy of Sciences, Wuhan, Hubei 430071, China
[d] School of Biomedical Engineering, Hainan University, Haikou 570228, Hainan, China.

ARTICLE INFO

Keywords:
Ultra-low-field (ULF) NMR
Nuclear magnetic relaxation dispersion (NMRD)
Optically pumped magnetometers (OPMs)
Shuttling NMR

ABSTRACT

Nuclear magnetic relaxation dispersion (NMRD) measurements report on molecular dynamics via the field-dependence of longitudinal (R_1) and transverse (R_2) relaxation rates. Commercial fast-field-cycling (FFC) relaxometers cover the kHz to MHz regime using large electromagnets, but show reduced sensitivity at lower frequencies. Optically pumped magnetometer based ultra-low-field (ULF) methods are highly sensitive to low frequencies (Hz to kHz), making them sensitive to slow molecular dynamics, but are restricted to the sub-kilohertz band. In this work, we introduce a compact shuttle-based relaxometry system that combines high-field prepolarization with programmable relaxation fields from nanotesla to tesla, and uses a set of multi-channel optically pumped magnetometers for arrayed detection. To benchmark the system's sensitivity and reproducibility we performed initial experiments on water samples, and then studied the field-dependent relaxivity of Gd-DTPA. These results agree quantitatively with a commercial FFC relaxometer across the accessible frequency range of three orders of magnitude (10 kHz to 20 MHz), and our setup extended the measurement range to eight orders of magnitude (Hz to 100 MHz). We also performed measurements on aqueous metal–organic framework solutions, highlighting the ability of ULF detection to mitigate susceptibility-induced internal field gradients. This platform enables wide-range, quantitative relaxometry, naturally interfaces with low-field hyperpolarization and supports applications in biomedical sensing of contrast agents and metabolites, porous-media and materials studies, and on-site chemical screening.

1. Introduction

Nuclear magnetic resonance (NMR) spectroscopy traditionally exploits chemical shifts and J couplings to extract structural and chemical information. An equally important source of contrast, however, arises from nuclear spin relaxation rates [1,2]. Relaxometry—the measurement of longitudinal (R_1) and transverse (R_2) relaxation rates as a function of magnetic fields—links frequency-dependent relaxation to underlying molecular dynamics, dipolar interactions, and exchange processes [3,4]. The resulting nuclear magnetic relaxation dispersion (NMRD) profiles provide sensitive, model-based probes of molecular motion and local environments [5,6].

Because of this mechanistic grounding, relaxometry has broad scientific and practical impact. In food science, it enables quantitative metabolite profiling, authenticity assessment, and evaluation of processing and storage quality [7]. In geoscience, relaxometry of confined liquids in porous media provides insights into pore geometry [8] and adsorption processes [9,10]. In medicine, field-dependent relaxometry

* Corresponding author at: State Key Laboratory of Magnetic Resonance Spectroscopy and Imaging, National Center for Magnetic Resonance in Wuhan, Wuhan Institute of Physics and Mathematics, Innovation Academy for Precision Measurement Science and Technology, Chinese Academy of Sciences – Wuhan National Laboratory for Optoelectronics, Huazhong University of Science and Technology, Wuhan 430071, Hubei, China.
E-mail address: xinzhou@wipm.ac.cn (X. Zhou).
[1] These authors contributed equally to this work.

https://doi.org/10.1016/j.jmr.2026.108128
Received 15 April 2026; Received in revised form 30 June 2026; Accepted 5 July 2026
Available online 16 July 2026

guides the design and characterization of MRI contrast agents [11], thereby enhancing diagnostic capabilities [12]. Together, these examples illustrate the versatility of relaxometry as both a mechanistic probe and a practical analytical tool.

The dominant experimental approach to measuring NMRD relies on fast-field-cycling (FFC) relaxometry, typically implemented with programmable electromagnets and inductive detection [13–15]. Commercial FFC relaxometers are established platforms for quantitative NMRD measurements, particularly over kHz–MHz proton Larmor frequencies. However, extending toward the ultralow-frequency regime and broad-range electromagnetic field cycling can be technically demanding because field-settling transients, low-frequency noise, field calibration, power electronics, and thermal management become increasingly important [5]. Wide-range field cycling with electromagnets typically necessitates dedicated power electronics and cooling infrastructure to manage thermal dissipation, which can limit the portability of conventional FFC instruments and increase operational complexity [16]. Mechanical sample shuttling provides another established route, in which the sample is physically transferred between magnetic-field regions so that spin evolution and detection can occur under different field conditions. Early high-resolution field-cycling and sample-shuttling approaches, together with subsequent biomolecular relaxometry platforms, established the use of mechanical transfer for separating low- or intermediate-field spin evolution from NMR readout [17–19]. More recent pneumatic [20], benchtop [21], gear-rod [22], and compact broad-range field-cycling systems [23] have further demonstrated automated sample transfer and broad field coverage. However, many of these implementations still rely on RF excitation and inductive readout. This can be restrictive for metal-enclosed samples, where RF attenuation is important, and for strongly heterogeneous samples when spectral linewidth or high-resolution readout is required [5,24]. Thus, ultra-wide field access itself is not unique to the present work. These considerations motivate complementary architectures that combine field-cycling capability with direct low-field magnetometer readout.

In parallel, ultra-low-field nuclear magnetic resonance (ULF NMR) has matured into a powerful technique for characterizing spin precession in the hertz-to-kilohertz domain [25–27]. This development has been enabled by substantial progress in magnetometry, which enables sensitive detection at low frequencies [28,29]. Among non-inductive approaches, optically pumped magnetometers (OPMs) have proven particularly capable [30,31]. When operated in magnetically shielded environments, OPMs directly measure magnetic fields generated by the sample, thereby circumventing the low-frequency sensitivity roll-off inherent to inductive coils. They further provide high near-DC sensitivity with broadband sub-kilohertz coverage, compact and low-power instrumentation, room-temperature (non-cryogenic) operation, and favorable cost and deployability [32–34]. In a relaxometry context, low- and ultralow-field R_1 measurements report on the spectral density of molecular and spin-environment fluctuations near the corresponding Larmor frequencies [6,35]. The connection between molecular dynamics and R_1 relaxation is mechanism-dependent: processes that modulate dipolar, paramagnetic, exchange-related, or other relaxation-active spin interactions that remain effective at low field can contribute to relaxation [36]. However, ULF detection alone does not provide independent control over relaxation fields across the kHz–MHz Larmor-frequency range. Without auxiliary field-cycling or shuttling hardware, ULF platforms therefore cannot by themselves map relaxation dispersion across the broader frequency window in which molecular tumbling, exchange, and paramagnetic relaxation mechanisms often show substantial field dependence [3,29,37].

Clinically used gadolinium chelates such as gadolinium diethylenetriaminepentaacetic acid (Gd-DTPA) are widely regarded as benchmark systems for NMR relaxometry and MRI contrast agent studies [11]. Their longitudinal relaxivity has been systematically characterized across broad field ranges using conventional FFC methods, as well as by low-field detection with atomic magnetometers [38,39]. Moreover, extensive work has established the physicochemical factors controlling their field-dependent relaxivity and strategies for enhancing sensitivity [40]. Consequently, Gd-DTPA is an ideal test case to validate the performance of new relaxometry platforms.

Here we present an OPM-detected shuttle NMR relaxometry system that directly bridges the gap between conventional FFC and ULF approaches by combining high-field prepolarization, wide-range programmable relaxation fields, and zero-field detection with a compact multi-channel OPM array. In this design, samples are motor-driven along a fixed path between a 2 T permanent magnet and a magnetically shielded detection region. Relaxation fields are provided by flat solenoid electromagnets, or permanent magnets, covering nearly nine orders of magnitude in Larmor frequency.

We validated the platform using a set of representative systems. First, we measured the relaxivity of the clinically used contrast agent Gd-DTPA and found excellent agreement with both commercial FFC relaxometers and literature values [40]. Second, we examined field-dependent water relaxation in a conductive titanium sample tube, and found that the shuttle sequence yields consistent R_1 profiles with only modest deviations from a standard glass tube, despite a strong contrast in the magnetic susceptibility at the metal–solution interface. Finally, we compared high-field and ultralow-field measurements of ammonium solutions containing metal–organic framework (MOF) particles. At 400 MHz the heterogeneous MOF induces severe susceptibility-driven line broadening, whereas at ULF the transverse relaxation remains only weakly concentration-dependent, underscoring the robustness of zero-field detection in the presence of highly inhomogeneous materials. Together, these demonstrations highlight that the shuttle-based system can perform quantitative relaxometry in conventional solutions, within metal hardware, and in strongly heterogeneous porous media, opening opportunities for in situ studies of catalytic reactors, electrochemical cells, and implant-compatible biomedical sensing.

2. Materials and methods

2.1. Experimental apparatus

The shuttle NMR platform couples three relaxation-field modules to a (near-)zero-field detection chamber (Fig. 1A). Relaxation fields are provided by (i) a flat solenoid for ULF (nT–hundreds of μT, corresponding to sub-Hz to kHz ^{1}H Larmor frequencies), (ii) an electromagnet for low-to-intermediate fields (up to ~10 MHz ^{1}H Larmor, 0.235 T), Higher-frequency relaxation points were obtained using the calibrated field profile of the 2 T permanent magnet and its fringe-field region along the shuttle path (See Supplementary Fig. 4), and (iii) a permanent magnet for high-field operation (tens of MHz). Following the relaxation period, samples are delivered into a four-layer magnetic shield for readout by a six-channel OPM array. The detection array comprises five home-built magnetometers and one commercial QuSpin QZFM Gen-2 sensor (designated as Ch1), their performance characteristics are compared in the Supporting Information **(see Supplementary Fig. 3)**. The six-channel configuration was chosen as a practical compromise between the available shield volume, sensor dimensions, electronic/optical access, and the need for redundant detection. The array enabled channel-to-channel comparison, exclusion of poor-quality channels when necessary, and averaging of suitable channels to improve measurement robustness. Commercial FFC reference measurements were performed using a Stelar Spinmaster FFC2000 NMR relaxometer (Stelar, Italy), as detailed in the Supplementary Information.

The ULF solenoid is driven by a Keithley 6221 precision current source, enabling low-ripple DC biases and fast, programmable ramps for kHz-range relaxation points. A separate transverse pulse coil, labeled in Fig. 1A, was used to generate the π/2 tipping pulse. An FPC shim-coil set mounted on the innermost shield layer provided x-, y-, and z-field compensation and first-order shimming during OPM detection. The electromagnet is powered by an AE Techron 7224 broadband power

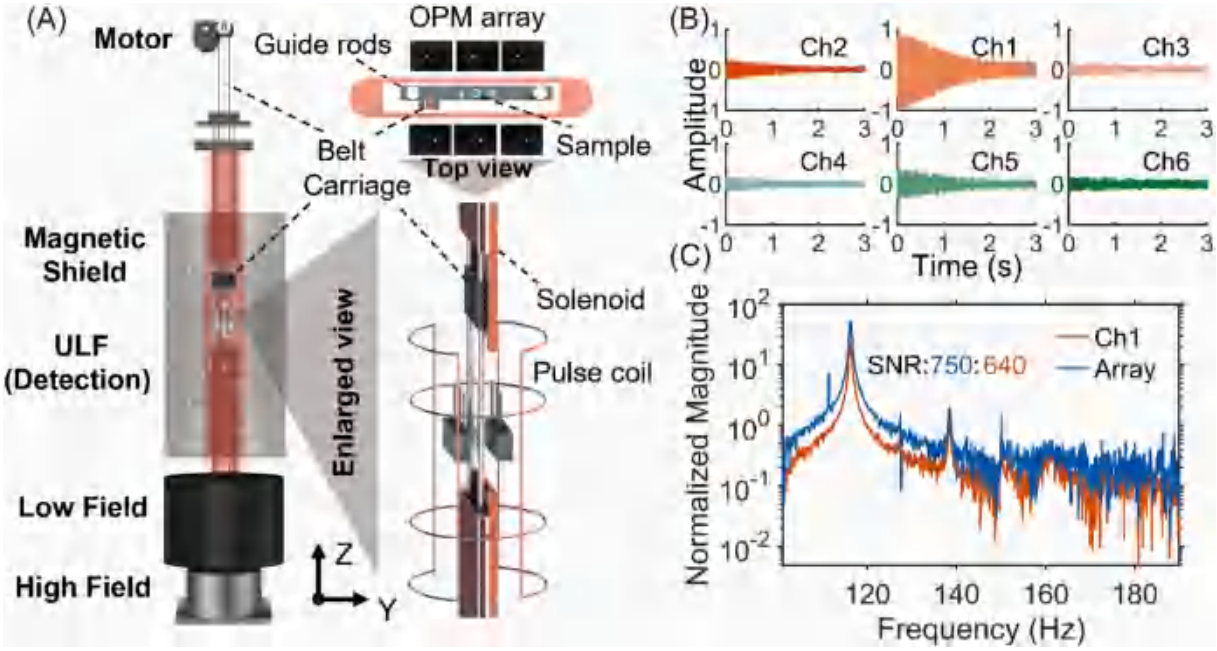

Fig. 1. Experimental schematic of the relaxometry system. **(A)** Schematic of the shuttle-based system showing the sample path between the high-field region, a low-field electromagnet region, and the ULF detection region with a multi-channel OPM array. The enlarged view shows the NMR tube fixed in a 3D-printed carriage guided by fiberglass rods and driven by a timing belt for motorized transfer between the relaxation-field modules and the shielded OPM detection region. **(B)** Representative free induction decay (FID) signals of water recorded simultaneously from six OPM channels. **(C)** Frequency-domain SNR comparison between the Ch1 (orange, SNR ~640) and the optimized six-channel array (blue, SNR ~750). (For interpretation of the references to colour in this figure legend, the reader is referred to the web version of this article.)

amplifier whose input is generated and gated by a NI-6281 DAQ. This pathway provides amplitude/frequency agility for 10 kHz–10 MHz relaxation fields. High-field points (>10 MHz) are obtained with the lower permanent magnet using the DP sequence. All timing, coil currents, and TTL triggers are orchestrated in LabVIEW, which also logs all experimental parameters for each cycle. Sample transfer was performed using a motor-driven belt shuttle. The NMR tube was fixed in a 3D-printed sample carriage, which was guided by two straight fiberglass rods passing through holes on both sides of the carriage to constrain the shuttle trajectory and suppress lateral motion. One side of the carriage was attached to a reinforced timing belt (5 M tooth, 3 mm width, 3 m total length) driven by a servo motor with braking (Mitsubishi HG-KR43BJ) through a 1:1.5 gear ratio and a Ø12 mm drive gear. The belt-driven mechanism translated the sample reproducibly between the solenoid, electromagnet, permanent-magnet region, and shielded OPM detection region, with a transfer time of 200 ms and sub-millimeter positional repeatability. Detailed carriage geometry, photographs with dimensions, and measured magnetic-field profiles along the shuttle path are provided in the Supporting Information (**Supplementary Figs. 2, 4, 8 and 9**), including the determination of the optimal detection and polarization positions. In the coordinate system used in Fig. 1A, the flat solenoid and electromagnet fields are oriented predominantly along z, whereas the 2 T permanent magnet field is oriented along x. The shuttle trajectory and field profile were calibrated to ensure reproducible transfer and to minimize signal loss from uncontrolled precession during motion.

The shuttle, current sources/amplifier, and OPM acquisition are TTL-synchronized (LabVIEW/NI-6281), with the total duration set by the choice of storage delay τ_{var}. Typical values are a shuttle time of ~200 ms, a post-pulse dead time of ~40 ms, and an acquisition window of ~10 s. For in-shield relaxation fields whose proton Larmor frequencies were within the OPM detection bandwidth, the same field was used during both the relaxation delay and OPM readout. For in-shield relaxation fields outside this bandwidth, the solenoid current is rapidly ramped down just before the π/2 excitation and readout, so that the resulting OPM-detected free induction decay (FID), i.e., the time-domain free-precession signal of the sample magnetization, falls within the OPM band (0–350 Hz).

2.2. Shuttle relaxometry sequences

Longitudinal relaxometry on the OPM-detected shuttle NMR relaxometry system is performed using two standard field-cycling sequences, corresponding to the schemes shown in Fig. 2A. For ULF and low-field measurements, a pre-polarized sequence is used: the sample is polarized at high field for a time T_{pol}, shuttled to the chosen relaxation field B_{relax} via a transfer interval τ_{rel}, and allowed to relax for a variable storage time τ_{var}. The sample is then moved into the shielded ULF region, where a calibrated π/2 pulse (~10 μT, y-axis) is applied (see **Supplementary Figs. 2** and **4** for pulse duration calibration in the SI) and the FID is recorded with the OPM array, yielding attenuation curves as a function of τ_{var}. For high-field points, a depolarized (DP) sequence is employed: the sample magnetization is first reset to $M \approx 0$ during a depolarized period T_{depol} in the shielded near-zero-field region, and then shuttled to the target relaxation field and allowed to recover for a variable delay τ_{rec}, after which the sample is rapidly transferred to the ULF detector and read out with a π/2 pulse. In this case, recovery curves versus τ_{rec} report the high-field R_1. Unless otherwise stated, T_{pol} and $T_{depol} = 20$ s, corresponding to $\geq 5\,T_1$ for the reference samples under the respective conditions.

2.3. Multi-channel signal processing

To fully harness the spatial redundancy of the six-channel OPM array, individual time-domain signals were first detrended and transformed into the frequency domain. A complex multi-peak Lorentzian model was fitted to each channel to extract the signal amplitude (A_i), frequency, and phase (ϕ_i). To eliminate destructive interference during array integration, the true phase of each channel was corrected, and the spectra were coherently summed using an optimal weighting scheme.

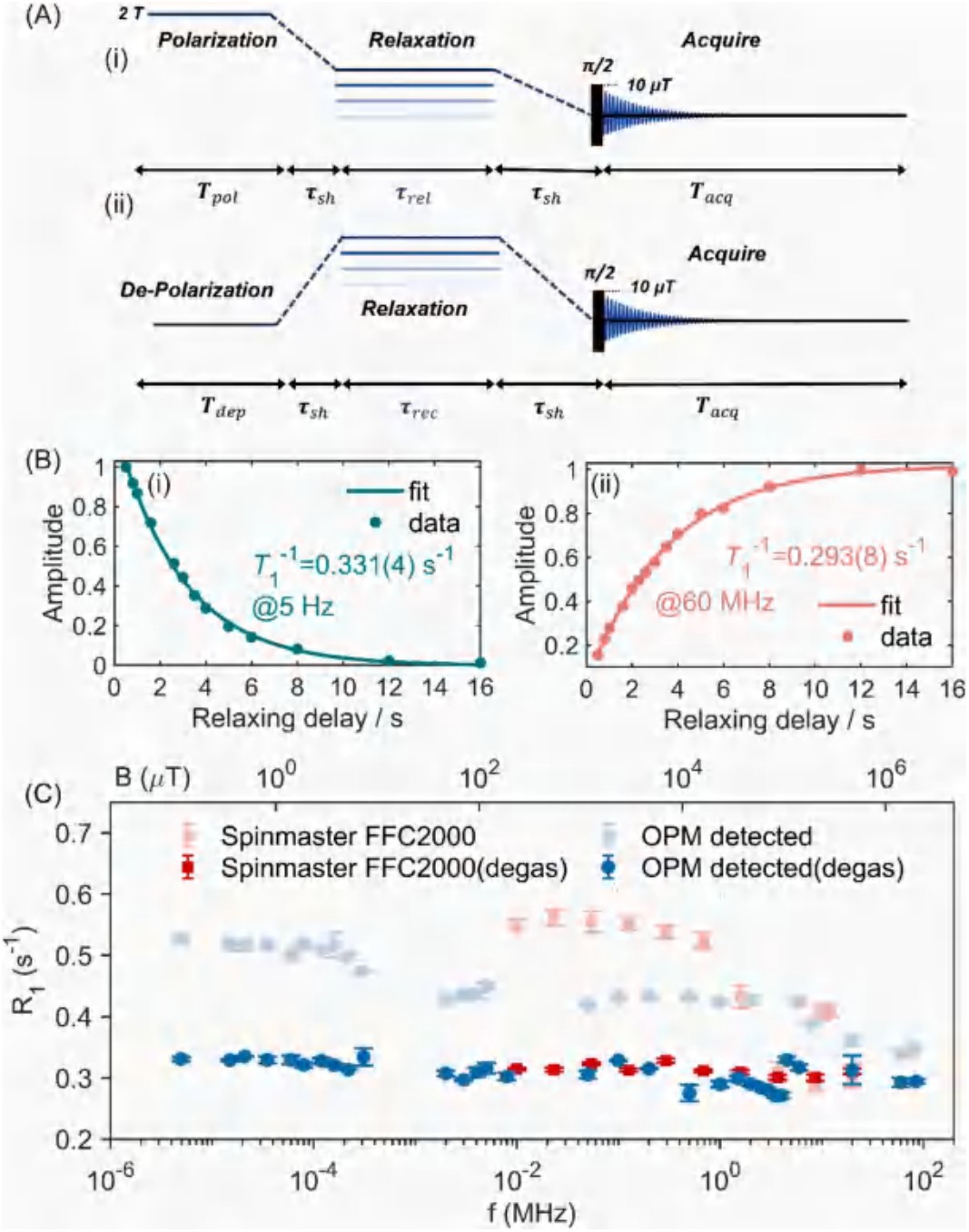

Fig. 2. Field-dependent relaxation measurements of water. **(A)** Pulse sequences used for longitudinal relaxation measurements. Two types of sequences were implemented: (i) polarization sequence for ULF/LF relaxometry. (ii) De-polarization sequence for high-field T_1 measurements. See Methods for full timing details. **(B)** Single-exponential fits describe both the decay (i) and recovery (ii) curves at 24 °C. **(C)** Summary of water relaxation rates with magnetic field strength. Blue symbols denote measurements obtained with the OPM-detected shuttle NMR relaxometry system, and red symbols denote measurements obtained with the Stelar Spinmaster FFC2000 relaxometer. Pale symbols indicate the original water sample, whereas solid symbols indicate deoxygenated samples. The comparison shows improved agreement between the two instruments after controlled deoxygenation. (For interpretation of the references to colour in this figure legend, the reader is referred to the web version of this article.)

The maximal-ratio combining (MRC) weights were defined as $w_i \propto A_i/\sigma_i^2$, where σ_i^2 is the high-frequency noise standard deviation of the i-th channel. The weights were further normalized by their L_2-norm ($w_i/\sqrt{\sum w_i^2}$) to ensure statistical consistency and rigorously quantify the array's sensitivity gain.

2.4. Sample preparations

Gd-DTPA (Adamas, 105819F) was dissolved in 10 mL deionized water to make a 10 mM stock solution and serially diluted to the working concentrations used in Fig. 3 (e.g., 0.05–0.25 mM), and the pH of the prepared solutions remained 7.4. Unless otherwise stated, samples were loaded into 5 mm tubes (sample volume ≈ 500 μL, and measured at room temperature (24 ± 0.1 °C).

Solutions of $^{14}NH_4Cl$ (Sigma-Aldrich, 213330) were first prepared at

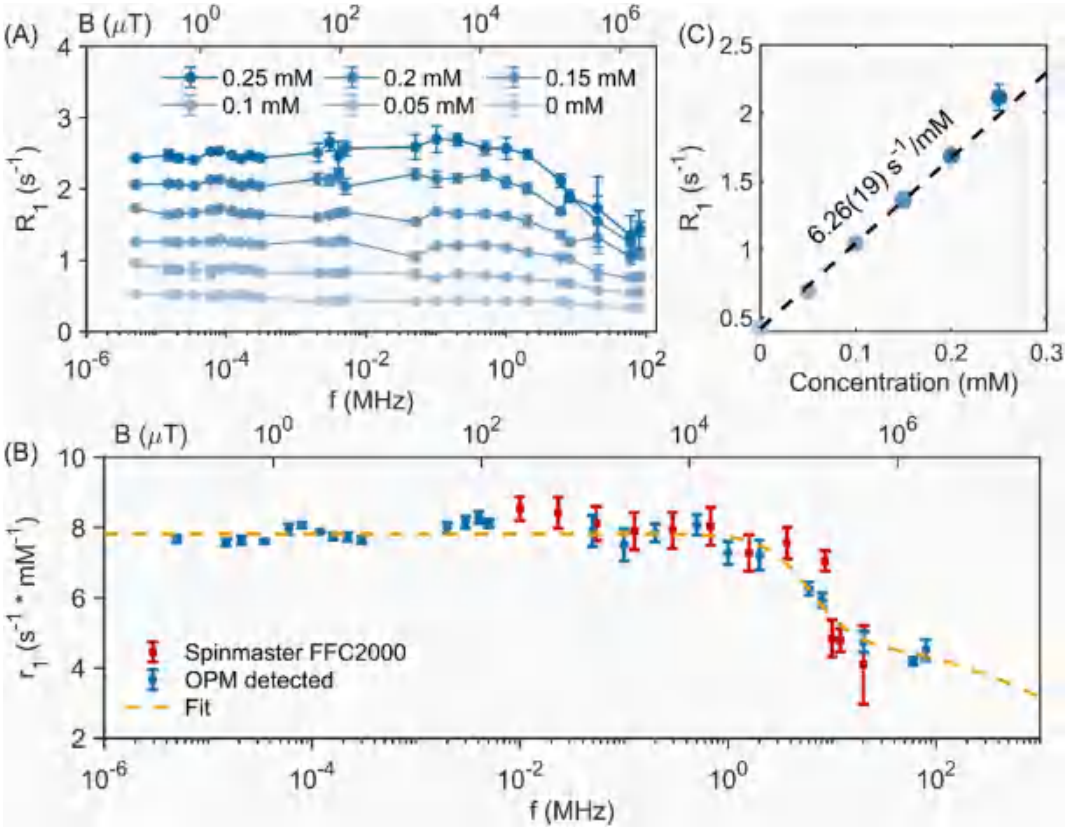

Fig. 3. Ultra-wide range shuttle NMR relaxometry of protons in aqueous Gd-DTPA. **(A)** Longitudinal relaxation rates R_1 of aqueous Gd-DTPA at 24 °C as a function of concentration for magnetic fields spanning <1 μT to 2 T. Each point represents the mean of four independent measurements, error bars denote the corresponding standard deviations. (**B**) Frequency-dependent longitudinal relaxivity r_1 as a function of proton Larmor frequency measured with the shuttle system (blue symbols) and with a commercial FFC relaxometer (red symbols). The dashed line shows the calculated relaxivity curve based on the SBM/Hwang–Freed model [42] using Eqs. S1–S14. The parameters used were $\tau_M = 23$ ns, $\tau_R = 131$ ps, $\tau_v = 8.53$ ps, $\Delta^2 = 12.9 \times 10^{19}$ s^{-2}, q = 1, $r = 3.41$ Å, D = 2.84×10^{-5} cm^2 s^{-1}, a = 4.16 Å, $r_{SS} = 3.94$ Å, $q_{SS} = 5.78$, and $\tau_{M,SS} = 17.2$ ps. **(C)** Representative linear regression of R_1 versus Gd-DTPA concentration at 6 MHz showing a linear dependence with slope $r_1 = 6.26$ (19) s^{-1} mM^{-1}. Symbols show experimental data and the solid line shows a linear least-squares fit. (For interpretation of the references to colour in this figure legend, the reader is referred to the web version of this article.)

6 M in deionized water. The pH was adjusted at room temperature by dropwise addition of 98% H_2SO_4 (Sigma-Aldrich) while monitoring with a calibrated pH meter, giving a final acid concentration of ≈1.9 M. For the MOF, CAU-1—an aluminum–amino terephthalate metal–organic framework with a three-dimensional porous structure (octahedral and tetrahedral cages of ~1.0 and 0.45 nm connected by 0.3–0.4 nm windows, Langmuir surface area ~ 1700 m^2 g^{-1}), was synthesized following the reported procedure [41] and dried at room temperature in air before use. The activated CAU-1 powder was gently ground and weighed into 5 mm NMR tubes, after which the NH_4Cl solution was added to obtain final CAU-1 loadings of 0, 100, and 150 mg/mL (sample volume ≈ 500 μL). The suspensions were vortexed and briefly sonicated to ensure homogeneous dispersion of the MOF particles, then equilibrated at room temperature for at least 5 min before high-field and ULF NMR measurements.

All deoxygenated samples were prepared using the same procedure after being loaded into their corresponding sample tubes. Each sample was placed under vacuum and then refilled with nitrogen. This vacuum/nitrogen cycle was repeated five times. The tubes were sealed immediately after deoxygenation and measured on the same day to minimize reintroduction of dissolved oxygen.

2.5. Relaxivity model for Gd-DTPA

The field-dependent proton relaxivity of Gd-DTPA was analyzed within the Solomon-Bloembergen-Morgan (SBM) framework [42], in which the observed longitudinal relaxation rate is written as $R_1(\omega_I) = R_{1,w} + [Gd]r_1(\omega_I)$, with $r_1(\omega_I) = r_1^{IS}(\omega_I) + r_1^{OS}(\omega_I)$. Here $R_{1,w}$ denotes the diamagnetic background relaxation rate of water, whereas the paramagnetic contribution is decomposed into inner-sphere and outer-sphere terms. The inner-sphere component describes relaxation mediated by water molecules directly coordinated to Gd^{3+} and depends primarily on the hydration number q, the residence lifetime of the bound water τ_m, the rotational correlation time τ_R, the Gd—H distance r_{IS}, and electron-spin relaxation parameters. Because proton-electron scalar coupling is small for Gd-DTPA, only the dominant dipolar contribution was retained. The outer-sphere term accounts for diffusional encounters between bulk water and the paramagnetic complex and was modeled using the Hwang-Freed formalism, parameterized by the relative diffusion coefficient D and the closest-approach distance d. Simultaneous fitting of the NMRD profile was performed by varying q, τ_m, τ_R, τ_v Δ^2, r_{IS}, D, and d within physically reasonable bounds to reproduce the experimental $r_1(\omega)$ (curve)

Relaxation rates were obtained by fitting the signal amplitudes as a function of relaxation delay to a single-exponential model. Uncertainties in fitted R_1 values were estimated by bootstrap resampling of the experimental data, and are reported as 95% confidence intervals unless otherwise stated.

3. Results

3.1. Design and performance of the shuttle NMR relaxometry

We characterized the baseline performance of the OPM-detected shuttle NMR relaxometry system using a 500 μL water sample. At a proton Larmor frequency of 116 Hz (B ≈ 2.7 μT, Fig. 1C), the QuSpin QZFM Gen-2 sensor (Ch1) achieves a single-scan SNR of 640. To further enhance sensitivity, we implemented a multi-channel detection scheme using the six-channel detection scheme.

However, we observed that a simple unweighted summation of all channels often resulted in a sub-optimal SNR, or even a decrease in signal quality. This is primarily due to destructive phase interference and severe amplitude disparities caused by the steep $1/r_i^3$ spatial decay of the sample's magnetic dipole field. To address this, we employed a phase-corrected Maximal-Ratio Combining (MRC) summation approach. Rather than relying solely on estimated geometric corrections, each channel was rotated by its true phase—extracted from frequency-domain Lorentzian fitting—to ensure strictly constructive interference. The aligned spectra were then coherently summed using optimal weights proportional to their individual signal-to-noise ratio squared (i.e., weight $\propto A/\sigma^2$).

This optimized coherent summation yielded an array SNR of ~750, demonstrating a 1.15-fold enhancement over the best individual sensor. While the peak amplitude theoretically approaches a $\sqrt{N}$ scaling when combining N identical and independent channels, the spatial dependency of ultra-low-field NMR concentrates the vast majority of the magnetic flux into the proximal sensor, causing inevitable deviations from the ideal $\sqrt{N}$ gain. Notably, the empirical array gain of 1.15× demonstrates that the multi-channel summation effectively enhances detection sensitivity. This performance indicates that the combining scheme effectively prioritizes the high-quality signal from proximal sensors while simultaneously facilitating the partial cancellation of spatially correlated environmental noise within the magnetic shield.

Using the two field-cycling sequences described in the Methods and summarized in Fig. 2A, we performed longitudinal relaxometry over a broad range of fields. For ULF and low-field measurements we use a pre-polarization sequence, whereas for high-field points a depolarized (DP) sequence probes relaxation directly at the target field before rapid transfer to the ULF detector. In all cases, the duty cycle is largely set by the storage delay τ_{var}, the polarization/depolarization durations and all field-switching, transport, and acquisition timings are specified in the Methods. The polarization and depolarization durations were chosen to be at least $5T_1$ of the sample at the corresponding field to ensure near-complete equilibration.

We extracted R_1 from stepped-τ series at two representative fields on degassed water at 24 °C. As shown in Fig. 2B **(i)**, at 5 Hz the signal decays mono-exponentially with τ, yielding $R_1 = 0.331(4)\ s^{-1}$ with $R^2 = 0.99$ and the residuals are structure-free. For 60 MHz (≈1.41 T), the DP variant gives $R_1 = 0.293(8)\ s^{-1}$ detected at 116 Hz proton Larmor frequency, again well described by a single-exponential model. Fig. 2C shows the water $R_1(B)$ dispersion from 5 Hz to 85 MHz acquired on the OPM-detected shuttle NMR relaxometry and compared with measurements from a Stelar Spinmaster FFC2000 relaxometer. The original datasets showed the same overall field-dependent trend over the overlapping range, but with a visible offset between the two instruments. To examine the role of sample oxygenation, we repeated the comparison using deoxygenated water samples measured on the same day at 24 °C. With this controlled sample preparation, the OPM-detected shuttle NMR relaxometry showed substantially improved agreement, with water T_1 values close to 3 s over the overlapping field range. These results confirm the consistency between the OPM-detected shuttle NMR relaxometry and commercial FFC relaxometry, while also showing that dissolved oxygen has a measurable influence on relaxation measurements.

All deoxygenated samples were prepared using the same procedure after being loaded into their corresponding sample tubes. Each sample was placed under vacuum and then refilled with nitrogen. This vacuum/nitrogen cycle was repeated five times. The tubes were sealed immediately after deoxygenation and measured on the same day to minimize reintroduction of dissolved oxygen.

3.2. Relaxometry of Gd-DTPA in an ultra-wide field range

We therefore evaluated the shuttle-based relaxometry platform using aqueous Gd-DTPA solutions at 24 °C. Measurements were performed on 500 μL samples at several concentrations over a magnetic-field range from ~70 nT to 2 T (proton Larmor frequencies from a few hertz to tens of megahertz). Each data point in Fig. 3A represents the average of four independent runs, demonstrating the reproducibility of the platform. The results show that R_1 increases approximately linearly with Gd-DTPA concentration across the full range, consistent with paramagnetic relaxation enhancement. However, the field dependence of R_1 differs between regimes. At ULF below ~10 kHz proton Larmor frequency, R_1 remains nearly constant, whereas in the low- to high-field range (kHz–MHz), R_1 exhibits a clear decrease with frequency. This behavior reflects the spectral-density profile of paramagnetic fluctuations: efficient dipolar relaxation at intermediate frequencies and reduced efficiency at both very low and very high frequencies.

To assess quantitative accuracy, we calculated relaxivity values ($r_1 = \Delta R_1/[\mathrm{Gd}]$) and compared them with results obtained from a commercial FFC NMR relaxometer. Despite fundamental differences in implementation—mechanical shuttling with OPM-based detection versus electronic field switching with inductive detection—both instruments probe the same underlying principle of field-cycled R_1 measurement. As shown in Fig. 3B, the relaxivity curves obtained with the shuttle NMR system and the commercial FFC instrument are in excellent agreement, particularly in the low-field regime where dispersion effects are most pronounced. As a representative example of this extraction procedure, the linear fit at 6 MHz (Fig. 3C) yields $r_1 = 6.26(19)\ s^{-1}\ mM^{-1}$,consistent with the literature NMRD profile, from which a value of 6.3 $mM^{-1}\ s^{-1}$ can be estimated [40]. These observations are consistent with earlier FFC relaxometry studies on paramagnetic agents and with magnetometer-based relaxometry of gadolinium complexes [39].

To further rationalize the field-dependent relaxivity and provide a quantitative interpretation of the NMRD profile, we calculated the $r_1(\omega)$ data using the Solomon–Bloembergen–Morgan (SBM) framework, in which the observed dispersion is decomposed into inner-sphere and outer-sphere contributions [40]. The calculation involved simultaneous optimization of key parameters governing water exchange, rotational and electronic dynamics, and diffusive encounters, yielding a theoretical curve that reproduces the experimentally measured NMRD behavior (Fig. 3B) (see Supporting Information for the full derivation and Eqs. 1–14). The fitted parameters and their 95% confidence intervals are summarized in Supplementary Table 1. These Gd-DTPA measurements provide a quantitative benchmark dataset for the OPM-detected shuttle NMR relaxometry system across the investigated field range and motivate the subsequent tests in metal-enclosed and heterogeneous samples.

3.3. Expanding sample compatibility to metal-enclosed systems

Relaxometry at ultralow field is intrinsically more tolerant to conductive enclosures, which are often problematic for conventional high-field NMR. To assess practical compatibility, we measured the longitudinal relaxation of water contained either in a standard 5 mm glass tube or in a 5 mm titanium tube (0.5 mm wall, ~500 μL). The field points were acquired in an interleaved order, and each R_1 value was obtained from four repeats and single-exponential fits with bootstrap errors.

As shown in Fig. 4, water R_1 values could be measured in both standard glass and titanium tubes over the investigated field range. The original measurements showed the same overall field-dependent trend

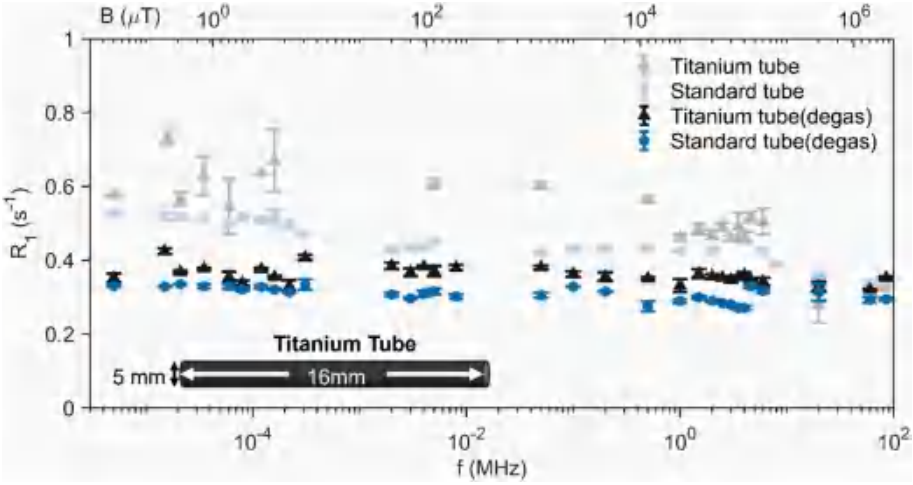

Fig. 4. Water R_1 across magnetic field in Titanium vs. standard glass tubes before and after deoxygenation. Black triangles: 5 mm titanium tube (0.5-mm-thick, ~500 μL). Blue circles standard glass tube. Pale symbols indicate the original measurements, whereas solid symbols indicate deoxygenated samples. Error bars represent bootstrap uncertainties from single-exponential fits. After deoxygenation, the offset between titanium- and glass-tube measurements is reduced but not completely eliminated. (For interpretation of the references to colour in this figure legend, the reader is referred to the web version of this article.)

but a visible offset between the two containers. After deoxygenation under matched preparation conditions, this offset was substantially reduced, indicating that dissolved oxygen contributed to the initial discrepancy. A small residual difference remained between the deoxygenated titanium- and glass-tube measurements, suggesting that container-related effects may still influence high-accuracy R_1 comparisons. These data demonstrate the feasibility of field-dependent relaxometry in a conductive titanium enclosure using the OPM-detected shuttle NMR relaxometry.

These measurements provide a metal-enclosed benchmark dataset

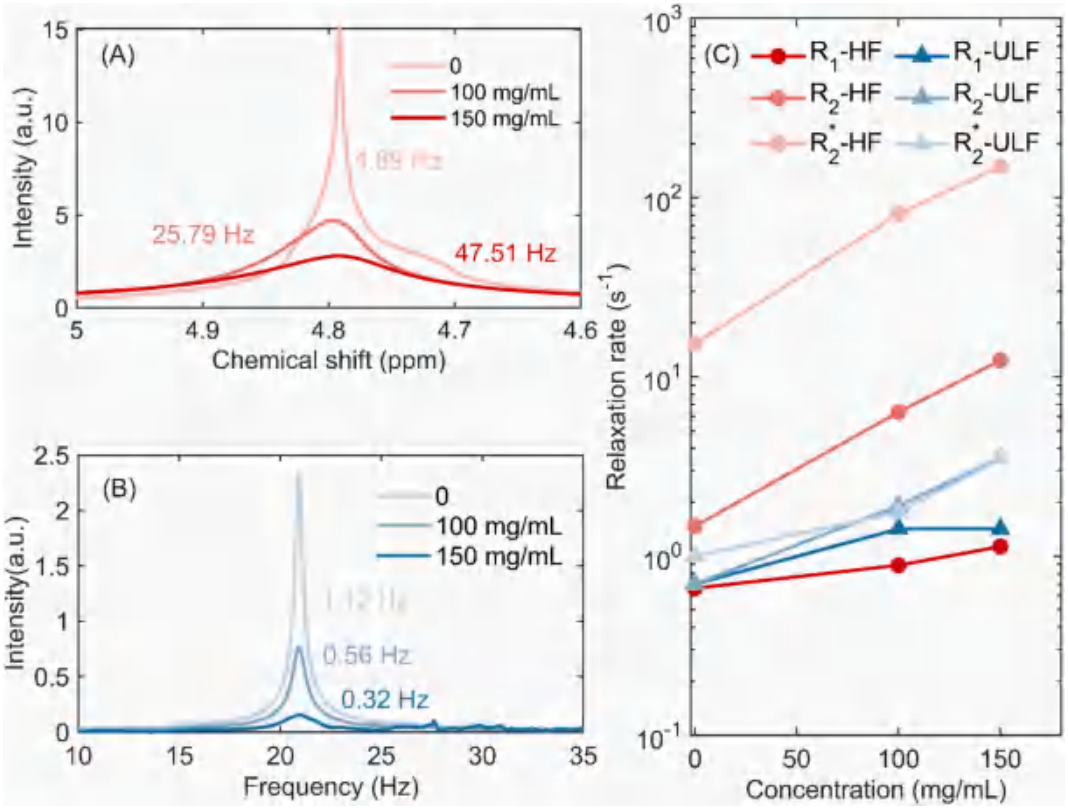

Fig. 5. Proton NMR linewidths of ammonium solutions with MOF additives measured at HF and ULF. **(A)** High-field (9.4 T) ^{1}H spectra of the water resonance in ammonium chloride solutions containing different concentrations of CAU-1 (0, 100, 150 mg/mL). The annotated values denote the full width at half maximum obtained from Lorentzian fits. **(B)** Corresponding ultralow-field ^{1}H spectra of the same samples acquired with the OPM-detected shuttle NMR relaxometry system under a background field corresponding to a proton Larmor frequency of 21 Hz. **(C)** Summary of R_1, spin-echo-derived R_2, and linewidth-derived R_2* relaxation rates measured at high field and ULF as a function of CAU-1 concentration. R_2 values were obtained from spin-echo decay measurements, whereas R_2* values were calculated from the Lorentzian linewidths in (A, B). Blue symbols denote HF data and red symbols denote ULF data. (For interpretation of the references to colour in this figure legend, the reader is referred to the web version of this article.)

and set the stage for the porous and heterogeneous-material experiments discussed next.

3.4. Suppression of susceptibility broadening in porous materials suspensions at ULF

Porous and heterogeneous materials typically generate strong internal susceptibility gradients, and conventional high-field NMRD experiments suffer from severe line broadening and loss of spectral resolution. To test how our shuttle-based platform performs under such conditions, we studied aqueous ammonium chloride solutions containing dispersed CAU-1, a nanoporous aluminum–amino terephthalate metal–organic framework with a three-dimensional pore network [41].

At 9.4 T (Fig. 5A), increasing the CAU-1 loading from 0 to 150 mg/mL produces strong susceptibility-induced broadening of the water resonance: the linewidth grows from 4.89 Hz to 25.79 and 47.51 Hz for 0, 100, and 150 mg/mL CAU-1, respectively, corresponding to linewidth-derived R_2* values of 15.36, 81.02, and 149.26 s^{-1} (Fig. 5C). Under these conditions, susceptibility-induced internal field gradients dominate the observed linewidth and apparent transverse dephasing, thereby restricting quantitative analysis. When the same samples are interrogated in the ultralow-field regime with the shuttle–OPM detector (Fig. 5B), the water peak remains narrow, with linewidths of 0.32, 0.56 and 1.12 Hz for 0, 100 and 150 mg/mL CAU-1, respectively, the corresponding R_2* values of 1.01, 1.76, and 3.52 s^{-1}.Fig. 5C further summarizes R_1, spin-echo-derived R_2, and linewidth-derived R_2* measured at HF and ULF. The ULF R_1 values were obtained under the same 21 Hz background field used for the spectra in Fig. 5B. The spin-echo-derived R_2 values were 1.47, 6.36, and 12.36 s^{-1} at high field and 0.70, 1.91, and 3.53 s^{-1} at ULF for 0, 100, and 150 mg/mL CAU-1, respectively. The much larger increase of R_2* relative to R_2 at high field indicates that the high-field spectra are dominated by susceptibility-induced inhomogeneous dephasing, whereas the smaller R_2/R_2* difference at ULF shows that near-zero-field detection substantially reduces susceptibility-induced linewidth broadening while preserving the concentration-dependent relaxation trend in heterogeneous suspensions of porous MOF particles.

4. Discussion

The shuttle-based NMR platform presented here demonstrates reliable performance for longitudinal relaxation measurements across an exceptionally wide magnetic-field range, from sub-μT to several tesla. Using water and Gd-DTPA—two widely studied relaxometry standards—we validated both the accuracy and sensitivity of the system. The integrated six-channel OPM array enhances detection sensitivity through coherent signal combination while retaining a compact footprint. The shielded ultralow-field detection region should not be interpreted as eliminating the requirement for magnetic-field homogeneity. Rather, the field homogeneity required for reproducible spin precession and linewidth control can be achieved without the high-order shimming typically used in high-resolution high-field spectroscopy. Relative to electromagnet-based commercial FFC relaxometers, the present implementation uses a shuttle geometry in which relaxation-field generation and ultralow-field magnetometer readout are physically separated. Similar separation of field evolution and detection has been adopted in previous mechanical field-cycling and shuttling system, including compact benchtop, robotic arms and gear-rack implementations [21,23,43,44]. The distinguishing feature of the present platform is therefore not the shuttling concept itself, but its integration with shielded multi-channel OPM detection for direct ultralow-field readout. Together with the metal-tube and MOF demonstrations, these results highlight quantitative performance while maintaining robustness to challenging sample environments.

The water measurements also illustrate the sensitivity of low-field relaxometry to sample preparation. In Fig. 2C, the original water datasets acquired with the OPM-detected shuttle NMR relaxometry and the commercial relaxometer showed the same field-dependent trend but a visible offset over the overlapping field range. After controlled deoxygenation and measurement at 24 °C, the two datasets showed substantially improved agreement, with water T_1 values close to 3 s. This comparison indicates that dissolved oxygen can measurably affect water R_1, consistent with the paramagnetic contribution of molecular oxygen to proton relaxation. Thus, oxygen control should be regarded as an essential part of quantitative water relaxometry, particularly when comparing measurements across different instruments or field-cycling platforms.

Another notable advantage of operating in the ULF regime is the reduced impact of RF skin-depth limitations during detection. In conventional high-field NMR, metallic enclosures can attenuate RF excitation and inductive signal reception, whereas the present platform detects nuclear magnetization directly with OPMs in a shielded ultralow-field region. Previous low-field and magnetometer-detected NMR studies have demonstrated the feasibility of measurements in metal-compatible sample environments [45], including conductive enclosures [46]. In the present titanium-tube experiment (Fig. 4), field-dependent R_1 values could be extracted from water inside the conductive enclosure. The non-deoxygenated measurements showed the same overall dispersion trend as the glass-tube reference but with a visible tube-dependent offset. After deoxygenation, this offset was markedly reduced, indicating that dissolved oxygen was a major contributor to the initial discrepancy. A residual difference between the deoxygenated titanium and glass tubes remains, particularly at lower relaxation fields. We therefore treat the titanium-tube result as a demonstration of feasible metal-enclosed sample container rather than as evidence of complete equivalence between the two containers. The residual offset may reflect container-wall-associated effects, including surface relaxation at the titanium/titanium-oxide interface, residual wall-bound oxygen or paramagnetic impurities, susceptibility differences between the metal wall and the liquid, or transient eddy-current fields during shuttling. Thus, matched sample preparation, oxygen control, and container-specific calibration remain necessary for quantitative comparisons.

Together, these results position the shuttle-based OPM relaxometry platform as a quantitative tool that bridges the ultralow-field and MHz regimes within a modular setup. By combining high-field prepolarization with magnetometer readout, the system complements commercial FFC relaxometry—particularly at very low fields and in challenging sample enclosures—while maintaining quantitative agreement in the overlap range. These combined features position the system to contribute both to fundamental studies of relaxation mechanisms and to contrast-agent characterization and development, as well as materials characterization.

Beyond metal-enclosed samples, porous and heterogeneous materials represent another important class of systems where conventional high-field NMRD is challenged by strong internal susceptibility gradients and restricted diffusion.

Previous ULF relaxometry studies using atomic magnetometers have shown that detecting imbibed liquids at fields below ~10 μT can minimize gradient-induced broadening and provide access to surface-induced relaxation and adsorption dynamics inside mesoporous silica pellets, even with chemical specificity via zero-field J-spectroscopy [26]. FFC ULF NMRD based on OPM detection has further demonstrated that such instruments can probe extremely slow correlation times in confined liquids and in metal tubing, across the nT–mT range that is difficult to reach with conventional FFC hardware [31]. The CAU-1 experiments reported here extend these ideas to suspensions of nanoporous metal–organic framework particles. Direct comparison of high-field and ULF transverse-decay behavior indicates that susceptibility-driven dephasing is substantially reduced under near-zero-field detection, while concentration-dependent relaxation trends remain observable. Nevertheless, the linewidth increase observed at ULF should not be regarded as negligible. Because spectral separations in low- and

ultralow-field NMR can occur on the hertz scale, for example through small Larmor-frequency differences or scalar-coupling splittings, Hz-level broadening may still affect spectral resolution in more complex low-field spectra. Taken together, these observations suggest that shuttle-based ULF relaxometry may provide a practical route to studying fluid dynamics and surface interactions in MOF-based catalysts, sorbents, and other complex porous media that are challenging to characterize using high-field NMR alone.

The mechanical transfer time is another practical limitation of the present implementation. In our current setup, transfer between the relaxation-field region and the OPM detection region takes 200 ms. For samples with T_1 values comparable to or shorter than this transfer time, magnetization may decay substantially during transfer, leading to reduced SNR and possible bias in the extracted relaxation rates. This effect is further complicated by the fact that the sample passes through a position-dependent magnetic-field profile during motion rather than remaining at a single well-defined relaxation field. The present platform is therefore most suitable for systems with relaxation times sufficiently longer than the transfer and field-settling times, or for measurements in which transfer-related relaxation can be explicitly calibrated or modeled.

The modest SNR gain of the six-channel array reflects the nonuniform contributions of different sensors. For a fixed sample position, the most effective SNR improvement may be obtained from sensors with high sensitivity and strong coupling to the sample field. Thus, the present six-channel layout should not be interpreted as an optimized sensor number for maximizing SNR. Instead, it increases the spatial detection region and allows comparison and selection among channels, consistent with recent multichannel ZULF NMR work using compact OPM arrays for spatially distributed detection [47].

Beyond these demonstrations, the same architecture offers a natural interface with hyperpolarization methods. Recent advances in parahydrogen-induced polarization (PHIP) and SABRE have highlighted that polarization-transfer and relaxation processes can show pronounced field dependence across low and intermediate magnetic fields. [48,49]. The ability to perform systematic relaxometry and spectroscopy across this field range makes this shuttle-based system well suited for optimizing and mechanistically studying hyperpolarization dynamics.

5. Conclusion

In summary, we have developed a shuttle-based NMR relaxometry platform that combines high-field prepolarization, programmable relaxation fields from the nanotesla to tesla regime, and multi-channel OPM detection at ultralow field within a single modular setup. Using water and Gd-DTPA as benchmarks, we demonstrated quantitative agreement with commercial FFC relaxometry across more than six orders of magnitude in proton Larmor frequency, establishing both the accuracy and sensitivity of the approach. Measurements in titanium tubes show that the system can reliably determine R_1 in metal-enclosed samples with small, quantitatively characterized deviations from standard glassware, extending relaxometry to applications that demand robust metallic housings. Experiments on ammonium solutions containing nanoporous CAU-1 further reveal that near-zero-field detection substantially suppresses susceptibility-induced broadening of the water resonance while retaining sensitivity to concentration-dependent relaxation, thereby helping to access intrinsic fluid and surface dynamics in heterogeneous porous suspensions. Together, these results position shuttle-based OPM relaxometry as a versatile tool for wide-range, quantitative relaxation studies in environments that are difficult for conventional high-field or FFC instruments, with promising prospects for biomedical sensing, catalysis and materials science. Future developments integrating hyperpolarization schemes or optimized shuttle trajectories may further enhance sensitivity and temporal resolution, broadening the range of accessible systems and experimental timescales.

CRediT authorship contribution statement

Qianyue Qu: Writing – review & editing, Writing – original draft, Visualization, Validation, Software, Methodology, Investigation, Formal analysis, Data curation. **Lianglin Tang:** Writing – review & editing, Visualization, Validation, Software, Investigation, Formal analysis, Data curation. **Zeming Li:** Software, Investigation. **Haogang Qi:** Investigation. **Li Wang:** Writing – review & editing, Validation, Software, Methodology, Formal analysis. **Liang Xu:** Investigation. **Qi Li:** Writing – review & editing. **Yunhuang Yang:** Writing – review & editing. **Yinan Hu:** Writing – review & editing, Project administration, Methodology, Funding acquisition, Conceptualization. **Xin Zhou:** Writing – review & editing, Supervision, Project administration, Funding acquisition, Conceptualization.

Funding

This work was supported by the National Key Research and Development Program of China (Nos. 2023YFF0714000 and 2022YFA1604501) and the National Natural Science Foundation of China (Nos. 82127802, 82441015 and U25D8004).

Declaration of competing interest

The authors declare that they have no known competing financial interests or personal relationships that could have appeared to influence the work reported in this paper.

Appendix A. Supplementary data

Supplementary data to this article can be found online at https://doi.org/10.1016/j.jmr.2026.108128.

Data availability statement

The raw data, processed relaxation-rate data, fitting results, and source data supporting the figures in this study have been deposited in Mendeley Data, V1, with the reserved DOI 10.17632/78kmhrm3py.1.

References

[1] R. Kimmich, NMR Tomography, Diffusometry, Relaxometry, 2019, https://doi.org/10.1007/978-3-642-60582-6.
[2] M.H. Levitt, Spin Dynamics: Basics of Nuclear Magnetic Resonance, 2 ed., John Wiley & Sons, Chichester, 2008.
[3] N. Bloembergen, E.M. Purcell, R.V. Pound, Relaxation effects in nuclear magnetic resonance absorption, Phys. Rev. 73 (1948) 679–712, https://doi.org/10.1103/PhysRev.73.679.
[4] S.H. Koenig, R.D. Brown, Field-cycling relaxometry of protein solutions and tissue: implications for MRI, Prog. Nucl. Magn. Reson. Spectrosc. 22 (1990) 487–567, https://doi.org/10.1016/0079-6565(90)80008-6.
[5] R. Kimmich, E. Anoardo, Field-cycling NMR relaxometry, Prog. Nucl. Magn. Reson. Spectrosc. 44 (2004) 257–320, https://doi.org/10.1016/j.pnmrs.2004.03.002.
[6] Field-cycling NMR Relaxometry: Instrumentation, model theories and applications, The Royal Society of Chemistry, 2018, https://doi.org/10.1039/9781788012966.
[7] B.P. Hills, Applications of low-field NMR to food science, in: G.A. Webb (Ed.), Annual Reports on NMR Spectroscopy, Academic Press, 2006, pp. 177–230, https://doi.org/10.1016/S0066-4103(05)58004-9.
[8] O.V. Bychuk, B. O'Shaughnessy, Anomalous Diffusion at Liquid Surfaces, Phys. Rev. Lett. 74 (1995) 1795–1798, https://doi.org/10.1103/PhysRevLett.74.1795.
[9] J.-C. Guo, H.-Y. Zhou, J. Zeng, K.-J. Wang, J. Lai, Y.-X. Liu, Advances in low-field nuclear magnetic resonance (NMR) technologies applied for characterization of pore space inside rocks: a critical review, Pet. Sci. 17 (2020) 1281–1297, https://doi.org/10.1007/s12182-020-00488-0.
[10] L.L. Barbosa, F.V.C. Kock, R.C. Silva, J.C.C. Freitas, V. Lacerda Jr., E.V.R. Castro, Application of low-field NMR for the determination of physical properties of petroleum fractions, Energy Fuel 27 (2013) 673–679, https://doi.org/10.1021/ef301588r.
[11] D.E.J. Waddington, T. Boele, R. Maschmeyer, Z. Kuncic, M.S. Rosen, High-sensitivity in vivo contrast for ultra-low field magnetic resonance imaging using superparamagnetic iron oxide nanoparticles, science, Advances 6 (2020) eabb0998, https://doi.org/10.1126/sciadv.abb0998.

[12] C. Johnson, N.L. Adolphi, K.L. Butler, D.M. Lovato, R. Larson, P.D.D. Schwindt, E. R. Flynn, Magnetic relaxometry with an atomic magnetometer and SQUID sensors on targeted cancer cells, J. Magn. Magn. Mater. 324 (2012) 2613–2619, https://doi.org/10.1016/j.jmmm.2012.03.015.
[13] C. Job, J. Zajicek, M.F. Brown, Fast field-cycling nuclear magnetic resonance spectrometer, Rev. Sci. Instrum. 67 (1996) 2113–2122, https://doi.org/10.1063/1.1147024.
[14] J. Ward-Williams, L.F. Gladden, Insights into adsorption behaviour of binary liquid mixtures in porous media using fast field cycling NMR, Magn. Reson. Imaging 56 (2019) 57–62, https://doi.org/10.1016/j.mri.2018.08.007.
[15] G. Ferrante, S. Sykora, Technical aspects of fast field cycling, in: Advances in Inorganic Chemistry, Academic Press, 2005, pp. 405–470, https://doi.org/10.1016/S0898-8838(05)57009-0.
[16] B. Kresse, A.F. Privalov, F. Fujara, NMR field-cycling at ultralow magnetic fields, Solid State Nucl. Magn. Reson. 40 (2011) 134–137, https://doi.org/10.1016/j.ssnmr.2011.10.002.
[17] A.G. Redfield, High-resolution NMR field-cycling device for full-range relaxation and structural studies of biopolymers on a shared commercial instrument, J. Biomol. NMR 52 (2012) 159–177, https://doi.org/10.1007/s10858-011-9594-1.
[18] C.Y. Chou, M.L. Chu, C.F. Chang, T.H. Huang, A compact high-speed mechanical sample shuttle for field-dependent high-resolution solution NMR, J. Magn. Reson. 214 (2012) 302–308, https://doi.org/10.1016/j.jmr.2011.12.001.
[19] K. Ivanov, A. Yurkovskaya, H.M. Vieth, High resolution NMR study of T₁ magnetic relaxation dispersion. I. Theoretical considerations of relaxation of scalar coupled spins at arbitrary magnetic field, J. Chem. Phys., 129 (2008). doi: https://doi.org/10.1063/1.3040272.
[20] P. TomHon, E. Akeroyd, S. Lehmkuhl, E.Y. Chekmenev, T. Theis, Automated pneumatic shuttle for magnetic field cycling and parahydrogen hyperpolarized multidimensional NMR, J. Magn. Reson. 312 (2020) 106700, https://doi.org/10.1016/j.jmr.2020.106700.
[21] F. Ellermann, P. Saul, J.-B. Hövener, A.N. Pravdivtsev, Modern manufacturing enables magnetic field cycling experiments and Parahydrogen-induced hyperpolarization with a benchtop NMR, Anal. Chem. 95 (2023) 6244–6252, https://doi.org/10.1021/acs.analchem.2c03682.
[22] I.V. Zhukov, A.S. Kiryutin, A.V. Yurkovskaya, Y.A. Grishin, H.-M. Vieth, K. L. Ivanov, Field-cycling NMR experiments in an ultra-wide magnetic field range: relaxation and coherent polarization transfer, Phys. Chem. Chem. Phys. 20 (2018) 12396–12405, https://doi.org/10.1039/C7CP08529J.
[23] J.P. Peters, C.D. Assaf, M. Côté, J.-B. Hövener, A.N. Pravdivtsev, Field cycling from 10 nT to 9.4 T: a flexible gear rod design for nuclear spin relaxation and hyperpolarization studies, ACS Meas. Sci. Au (2025), https://doi.org/10.1021/acsmeasuresciau.5c00131.
[24] E. Anoardo, G. Galli, G. Ferrante, Fast-field-cycling NMR: applications and instrumentation, Appl. Magn. Reson. 20 (2001) 365–404, https://doi.org/10.1007/BF03162287.
[25] P.J. Ganssle, H.D. Shin, S.J. Seltzer, V.S. Bajaj, M.P. Ledbetter, D. Budker, S. Knappe, J. Kitching, A. Pines, Ultra-low-field NMR relaxation and diffusion measurements using an optical magnetometer, Angew. Chem.-Int. Edit. 53 (2014) 9766–9770, https://doi.org/10.1002/anie.201403416.
[26] M.C.D. Tayler, J. Ward-Williams, L.F. Gladden, NMR relaxation in porous materials at zero and ultralow magnetic fields, J. Magn. Reson. 297 (2018) 1–8, https://doi.org/10.1016/j.jmr.2018.09.014.
[27] P. Volegov, M. Flynn, R. Kraus, P. Magnelind, A. Matlashov, P. Nath, T. Owens, H. Sandin, I. Savukov, L. Schultz, A. Urbaitis, V. Zotev, M. Espy, Magnetic resonance Relaxometry at low and ultra low fields, in: S. Supek, A. Sušac (Eds.), 17th International Conference on Biomagnetism Advances in Biomagnetism – Biomag2010, Springer Berlin Heidelberg, Berlin, Heidelberg, 2010, pp. 82–87.
[28] M.C.D. Tayler, T. Theis, T.F. Sjolander, J.W. Blanchard, A. Kentner, S. Pustelny, A. Pines, D. Budker, Invited review article: instrumentation for nuclear magnetic resonance in zero and ultralow magnetic field, Review of Scientific Instruments 88 (2017), https://doi.org/10.1063/1.5003347.
[29] Y.S. Greenberg, Application of superconducting quantum interference devices to nuclear magnetic resonance, Rev. Mod. Phys. 70 (1998) 175–222, https://doi.org/10.1103/RevModPhys.70.175.
[30] P. Put, S. Pustelny, D. Budker, E. Druga, T.F. Sjolander, A. Pines, D.A. Barskiy, Zero- to ultralow-field NMR spectroscopy of small biomolecules, Anal. Chem. 93 (2021) 3226–3232, https://doi.org/10.1021/acs.analchem.0c04738.
[31] S. Bodenstedt, M.W. Mitchell, M.C.D. Tayler, Fast-field-cycling ultralow-field nuclear magnetic relaxation dispersion, Nat. Commun. 12 (2021) 4041, https://doi.org/10.1038/s41467-021-24248-9.
[32] J.W. Blanchard, T. Wu, J. Eills, Y. Hu, D. Budker, Zero- to ultralow-field nuclear magnetic resonance J-spectroscopy with commercial atomic magnetometers, J. Magn. Reson. 314 (2020) 106723, https://doi.org/10.1016/j.jmr.2020.106723.
[33] J. Dupont-Roc, S. Haroche, C. Cohen-Tannoudji, Detection of very weak magnetic fields (10^{-9}gauss) by ^{87}Rb zero-field level crossing resonances, Phys. Lett. A 28 (1969) 638–639, https://doi.org/10.1016/0375-9601(69)90480-0.
[34] M. Batie, S. Bitant, J.F. Strasburger, V. Shah, O. Alem, R.T. Wakai, Detection of fetal arrhythmia by using optically pumped magnetometers, JACC: Clinical Electrophysiology 4 (2018) 284–287, https://doi.org/10.1016/j.jacep.2017.08.009.
[35] R. Kimmich, Field cycling in NMR relaxation spectroscopy: applications in biological, chemical and polymer physics, Bull. Magn. Reson. 1 (1980) 195–218.
[36] J.P. Peters, C. Assaf, A. Brahms, K. Them, M. Gerdsen, R. Herges, J.-B. Hövener, A. N. Pravdivtsev, Chemically induced deceleration of nuclear spin relaxation (CIDER) preserves hyperpolarization, science, Advances 11 (2025) eadx2316, https://doi.org/10.1126/sciadv.adx2316.
[37] D. Budker, M. Romalis, Optical magnetometry, Nat. Phys. 3 (2007) 227–234, https://doi.org/10.1038/nphys566.
[38] D.J. Michalak, S. Xu, T.J. Lowery, C.W. Crawford, M. Ledbetter, L.-S. Bouchard, D. E. Wemmer, D. Budker, A. Pines, Relaxivity of gadolinium complexes detected by atomic magnetometry, Magn. Reson. Med. 66 (2011) 603–606, https://doi.org/10.1002/mrm.22811.
[39] G. Liu, X. Li, X. Sun, J. Feng, C. Ye, X. Zhou, Ultralow field NMR spectrometer with an atomic magnetometer near room temperature, J. Magn. Reson. 237 (2013) 158–163, https://doi.org/10.1016/j.jmr.2013.10.008.
[40] P. Caravan, Strategies for increasing the sensitivity of gadolinium based MRI contrast agents, Chem. Soc. Rev. 35 (2006) 512–523, https://doi.org/10.1039/B510982P.
[41] T. Ahnfeldt, N. Guillou, D. Gunzelmann, I. Margiolaki, T. Loiseau, G. Férey, J. Senker, N. Stock, [Al4(OH)2(OCH3)4(H2N-bdc)3]·xH2O: a 12-connected porous metal–organic framework with an unprecedented aluminum-containing brick, Angew. Chem. Int. Ed. 48 (2009) 5163–5166, https://doi.org/10.1002/anie.200901409.
[42] L. Helm, Relaxivity in paramagnetic systems: theory and mechanisms, Prog. Nucl. Magn. Reson. Spectrosc. 49 (2006) 45–64, https://doi.org/10.1016/j.pnmrs.2006.03.003.
[43] K. Sheberstov, E. Van Dyke, J. Xu, R. Kircher, L. Chuchkova, Y. Hu, S. Alvi, D. Budker, D.A. Barskiy, Robotic arms for hyperpolarization-enhanced NMR, Journal of Magnetic Resonance Open 23 (2025) 100194, https://doi.org/10.1016/j.jmro.2025.100194.
[44] J. Yang, R. Xin, S. Lehmkuhl, J.G. Korvink, J.J. Brandner, Development of a fully automated workstation for conducting routine SABRE hyperpolarization, Sci. Rep. 14 (2024) 21022, https://doi.org/10.1038/s41598-024-71354-x.
[45] D.B. Burueva, J. Eills, J.W. Blanchard, A. Garcon, R. Picazo-Frutos, K.V. Kovtunov, I.V. Koptyug, D. Budker, Chemical reaction monitoring using zero-field nuclear magnetic resonance enables study of heterogeneous samples in metal containers, Angew. Chem. Int. Ed. 59 (2020) 17026–17032, https://doi.org/10.1002/anie.202006266.
[46] A.M. Fabricant, R. Picazo-Frutos, F. Teleanu, G.J. Rees, R. Kircher, M. Lin, W. Evans, P.-M. Luc, R.A. House, P.G. Bruce, P. Krüger, J.W. Blanchard, J. Eills, K. F. Sheberstov, R. Körber, D. Budker, D.A. Barskiy, A. Jerschow, Enabling nondestructive observation of electrolyte composition in batteries with ultralow-field nuclear magnetic resonance, Chem. Sci. 17 (2026) 5877–5887, https://doi.org/10.1039/D5SC04419G.
[47] B. Andrews, M. Lai, Z. Wang, N. Kato, M.C.D. Tayler, E. Druga, A. Ajoy, Sensitive multichannel zero-to ultralow-field NMR with atomic magnetometer arrays, PNAS Nexus 4 (2025), https://doi.org/10.1093/pnasnexus/pgaf187.
[48] J. Eills, R. Picazo-Frutos, O. Bondar, E. Cavallari, C. Carrera, S.J. Barker, M. Utz, A. Herrero-Gómez, I. Marco-Rius, M.C.D. Tayler, S. Aime, F. Reineri, D. Budker, J. W. Blanchard, Enzymatic reactions observed with zero- and low-field nuclear magnetic resonance, Anal. Chem. 95 (2023) 17997–18005, https://doi.org/10.1021/acs.analchem.3c02087.
[49] M. Gierse, L. Dagys, M. Keim, S. Lucas, F. Josten, M.B. Plenio, I. Schwartz, S. Knecht, J. Eills, Hyperpolarizing small molecules using Parahydrogen and solid-state spin diffusion, Angew. Chem. Int. Ed. 63 (2024) e202319341, https://doi.org/10.1002/anie.202319341.